

# Fully-frustrated octahedral antiferromagnet: emergent complexity in external field

A. S. Gubina,<sup>1</sup> T. Ziman,<sup>2,3</sup> and M. E. Zhitomirsky<sup>1,2</sup>

<sup>1</sup>Université Grenoble Alpes, CEA, IRIG, PHELIQS, 38000 Grenoble, France

<sup>2</sup>Institut Laue Langevin, 38042 Grenoble Cedex 9, France

<sup>3</sup>Kavli Institute for Theoretical Science, University of the Chinese Academy of Sciences, 100190, Beijing, China

(Dated: January 23, 2025)

Octahedral antiferromagnets are distinguished by crystal lattices composed of octahedra of magnetic ions. In the fully frustrated case, the Heisenberg Hamiltonian can be represented as a sum of squares of total spins for each octahedral block. We study the fully frustrated spin model for a lattice of edge-shared octahedra, which corresponds to the  $J_1$ - $J_2$  fcc antiferromagnet with  $J_2/J_1 = 1/2$ . The magnetization process at this strongly frustrated point features a remarkably rich sequence of different magnetic phases that include fractional plateaus at  $m = 1/3$  and  $2/3$  values of the total magnetization. By performing extensive Monte Carlo simulations we construct the  $H$ - $T$  phase diagram of the classical model with eight field-induced states, which acquire stability via the order by disorder mechanism. These antiferromagnetic states have distinct spin configurations of their octahedral blocks. The same spin configurations are also relevant for the fully frustrated corner-shared model bringing an apparent similarity to their field-induced states.

*Introduction.* — Geometrical frustration in a magnetic material occurs when the lattice topology prevents simultaneous minimization of all pairwise interactions between local moments. Frustrated spin models may possess accidental degeneracies, which lead to enhanced low-temperature fluctuations and, as a result, to a variety of new complex states [1–5]. Experimental and theoretical studies have so far focused on lattices based on triangular or tetrahedral spin units such as triangular, kagome, and pyrochlore antiferromagnets and their descendants [2].

Octahedral antiferromagnets constitute a distinct class of geometrically frustrated magnets that has received only limited attention to date. Magnetic ions in these materials form lattices composed of octahedral blocks. Two of such structures formed by corner- and edge-shared octahedra are presented in Figs. 1(a) and 1(b), respectively. The first type of magnetic lattice is realized in antiperovskites [6–8] and  $Mn_3X$  ordered alloys [9, 10]. The edge-shared octahedra are inherent to the face-centered cubic (fcc) structure and appear as elementary frustrated units in the  $J_1$ - $J_2$  antiferromagnetic fcc materials [11] at a fully frustrated point  $J_2/J_1 = 1/2$ , as detailed below. Recently, there have been a number of experimental [12–16] and theoretical [17–23] studies of octahedral materials and models with a focus on their unusual magnetic properties. In particular, complex  $H$ - $T$  phase diagrams have been measured for europium antiperovskites  $Eu_3PbO$  [14] and  $Eu_3SnO$  [15]. At low temperatures, their magnetization curves exhibit several plateau-like features, including one close to  $1/3$  of the total magnetization. Magnetic  $Eu^{2+}$  ions in both compounds have large semiclassical spins  $S = 7/2$ , typically with a weak magnetic anisotropy. In consequence, the magnetization plateaus in these materials can be a direct consequence of magnetic frustration in the octahedral lattice.

The frustrated units or blocks that make up a lattice

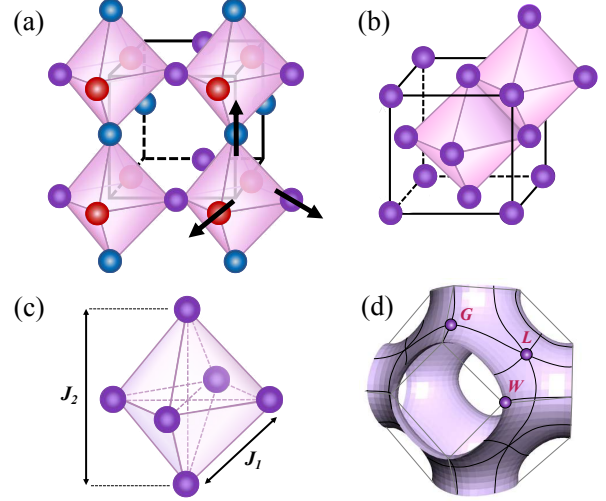


FIG. 1. Examples of octahedral lattices. (a) Corner-shared network realized in cubic antiperovskites. Colored spheres specify the  $q = 0$  antiferromagnetic state with the  $120^\circ$  arrangement of spins. (b) Edge-shared network emerging in the  $J_1$ - $J_2$  fcc antiferromagnet. (c) A spin octahedron with two types of exchange interactions. (d) Manifold of degenerate wavevectors corresponding to the minimum of  $J(\mathbf{q})$  in the Brillouin zone for the fcc model with  $J_2/J_1 = 1/2$ . Special symmetry points:  $L$  or  $\mathbf{Q}_2 = (\pi, \pi, \pi)$ ,  $W$  or  $\mathbf{Q}_3 = (2\pi, \pi, 0)$ ,  $G$  or  $\mathbf{Q}_4 = (4\pi/3, 0, 4\pi/3)$ .

influence the magnetization process of the corresponding antiferromagnetic model. In particular, the semi-classical magnetization plateaus depend on the number of spins in each block [24]. As a result, triangular and kagomé lattice antiferromagnets can exhibit plateaus at  $1/3$  of the total magnetization  $m_s$  [25–29], while the pyrochlore and  $J_1$ - $J_2$  square lattice antiferromagnets both show  $1/2$  magnetization plateaus [24, 30]. The lattice topology, edge-versus corner-shared units, affects the periodicity and degeneracy of emergent states and can lead to additional

quantum plateaus known as magnon crystals [29, 31–34].

In this Letter, we investigate the magnetization process of an octahedral antiferromagnet for both types of lattices shown in Fig. 1 with the isotropic exchange interactions:

$$\hat{H} = \sum_{\langle ij \rangle} J_{ij} \mathbf{S}_i \cdot \mathbf{S}_j - \mathbf{H} \cdot \sum_i \mathbf{S}_i. \quad (1)$$

Two kinds of exchange constants naturally appear for both models:  $J_1$  along octahedron edges and  $J_2$  connecting the opposite vertices, see Fig. 1(c). The magnetization plateaus can appear at  $m/m_s = 1/3$  and  $2/3$ . Surprisingly, we also find an abundance of stable non-collinear states in between, which produce intricate and complex phase diagrams. An example of such a diagram for the classical spins on the edge-shared octahedra network is shown in Fig. 2.

*Classical ground states.* — The lowest-energy magnetic states of the spin Hamiltonian (1) are obtained by treating  $\mathbf{S}_i$  as classical vectors of unit length. For a corner-shared lattice, the energy per single octahedron can be written as

$$E_{\text{oct}} = \frac{1}{2} [J_1 \mathbf{S}_{\text{tot}}^2 + (J_2 - J_1)(\mathbf{S}_{d1}^2 + \mathbf{S}_{d2}^2 + \mathbf{S}_{d3}^2) - \mathbf{H} \cdot \mathbf{S}_{\text{tot}}], \quad (2)$$

where  $\mathbf{S}_{\text{tot}}$  is the total spin of an octahedron unit and  $\mathbf{S}_{d_n}$  are sums of spins on diagonal bonds. For  $J_2 < J_1$ , pairs of diagonal spins remain parallel for all  $H$ , maximizing  $|\mathbf{S}_{d_n}| = 2$ . In zero field, the condition  $\mathbf{S}_{\text{tot}} = 0$  leads to a  $120^\circ$  arrangement of three vectors  $\mathbf{S}_{d_n}$ . The lowest energy state of a single unit also yields a ground state of the entire system by simple periodic repetition, Fig. 1(a). The  $q = 0$  triangular antiferromagnetic structure has been observed in several cubic materials consisting of octahedra [9, 10, 35]. Additional ground states are constructed from the  $q = 0$  structure by rotating two sublattices around the third one. Such rotations can be performed independently by different angles for spins in parallel square planes sandwiched between layers of the third sublattice, see Fig. 1(a). This continuous degeneracy is present for all  $J_2 < J_1$  and is consistent with degenerate lines  $(0, 0, q)$  in the momentum space for the lowest eigenvalue of the Fourier transform of the exchange matrix [36].

In an applied field, minimization of (2) yields the total magnetization of an octahedron unit

$$\mathbf{S}_{\text{tot}} = \mathbf{H}/(2J_1). \quad (3)$$

This condition can be satisfied below the saturation field  $H_s = 12J_1$  by a family of three-sublattice structures described by two continuous angle parameters. Similar to the case of a triangular-lattice antiferromagnet, quantum or thermal fluctuations favor the coplanar spin configurations via the order by disorder effect [25–27]. In particular, they stabilize the intermediate collinear up-up-down

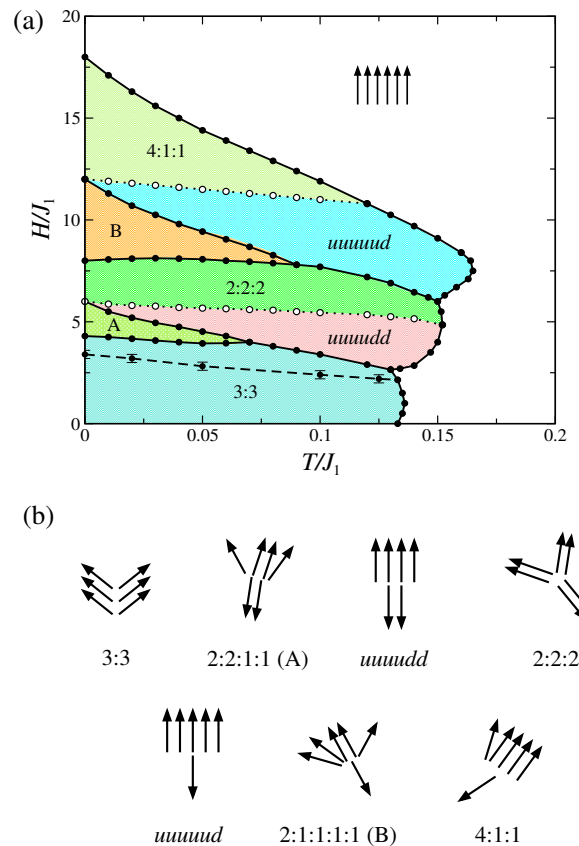


FIG. 2. (a) Phase diagram of the classical Heisenberg fcc antiferromagnet with  $J_2/J_1 = 1/2$ . (b) Octahedron spin configurations for each of the phases. Closed and open circles indicate first- and second-order transition points, respectively, as a guide to the eye. The dashed line and symbols inside the 3:3 phase indicate the first-order transitions with a change of the ordering wavevector from  $\mathbf{Q}_3$  at low fields to  $\mathbf{Q}_2$  at higher fields.

(*uud*) state producing the  $1/3$  magnetization plateau for all  $J_2 < J_1$ . Thus, the experimental observation of such a plateau in  $\text{Eu}_3\text{SnO}$  [15] is fully consistent with the antiferromagnetic nearest-neighbor interactions between Eu ions in the corner-shared octahedral lattice.

The classical degeneracy is greatly enhanced at the fully frustrated point  $J_2 = J_1$ . For equal couplings, any six-sublattice configuration satisfying (3) yields the ground state for all fields  $0 \leq H \leq H_s$ . Furthermore, the Maxwellian counting arguments [37] suggest a macroscopic degeneracy of the ground-state manifold for a lattice of corner-shared octahedra parameterized by  $N$  angles, where  $N$  is the total number of spins. Such a degeneracy corresponds to a flat band of zero energy modes in the momentum space [36] similar to kagome and pyrochlore antiferromagnets [37, 38]. This may lead to new interesting spin liquid states in zero field [21, 23].

The ordered states of the  $J_1$ – $J_2$  fcc antiferromagnet include the AF2 phase for  $J_2/J_1 > 1/2$  described by

the propagation wavevectors  $\mathbf{Q}_2 = (\pi, \pi, \pi)$  and the AF3 phase for  $0 < J_2/J_1 < 1/2$  with  $\mathbf{Q}_3 = (0, \pi, 2\pi)$  [11]. The degeneracy is enhanced at the boundary  $J_2/J_1 = 1/2$ , where the classical ground states are spin spirals satisfying

$$\cos \frac{Q_x}{2} + \cos \frac{Q_y}{2} + \cos \frac{Q_z}{2} = 0, \quad (4)$$

see Fig. 1(d) [39–41]. At this fully frustrated point, the block representation applies to the fcc model (1) with an octahedron energy

$$E_{\text{oct}} = \frac{1}{4} J_1 \mathbf{S}_{\text{tot}}^2 - \frac{1}{6} \mathbf{H} \cdot \mathbf{S}_{\text{tot}}. \quad (5)$$

The difference in the prefactors from Eq. (2) is due to edge-shared versus corner-shared stacking of octahedra. The lowest energy of a single octahedron block is obtained for

$$\mathbf{S}_{\text{tot}} = \mathbf{H}/(3J_1). \quad (6)$$

Just as for the corner-shared lattice, any six-sublattice configuration with a fixed magnetization (6) gives a classical ground state. Thus, two fully-frustrated octahedral models exhibit similar local degeneracy. In a magnetic field they can exhibit a rich variety of ordered magnetic structures stabilized by the effect of order by disorder [42, 43]. The block connectivity, edge vs. corner-shared, determines the ordering wavevectors and the additional degeneracy that may arise once six sublattices are distributed over the entire lattice.

*Single octahedron states.*—We begin by exploring possible magnetic states for a fully frustrated octahedron unit. Six-sublattice configurations satisfying (3) (or (6)) are parameterized by eight continuous variables, modulo a global rotation about  $\mathbf{H}$ . This leads to a significantly larger manifold of classical ground states compared to spin models based on triangles (two angles) or tetrahedra (four angles). Consequently, the selection of states by quantum or thermal fluctuations becomes a nontrivial problem.

Generally, the short-range quantum fluctuations can be taken into account by an effective biquadratic exchange [44–46]. Accordingly, we consider

$$\hat{\mathcal{H}}_{\text{biq}} = - \sum_{\langle ij \rangle} B_{ij} (\mathbf{S}_i \cdot \mathbf{S}_j)^2 \quad (7)$$

with two dimensionless constants  $b_{1,2} = B_{ij} S^2 / J_{ij}$  for the first ( $J_1$ ) and the second ( $J_2$ ) neighbor bonds. The second-order quantum correction to the ground state energy yields  $b_1 = 1/(24S)$ ,  $b_2/b_1 = 1/2$  for the fully-frustrated fcc model and  $b_1 = 1/(16S)$ ,  $b_2/b_1 = 1$  for the corner-shared lattice with  $J_2 = J_1$ , see [36]. For purely classical spin models, the low- $T$  contribution of the short-range thermal fluctuations can be also expressed in a

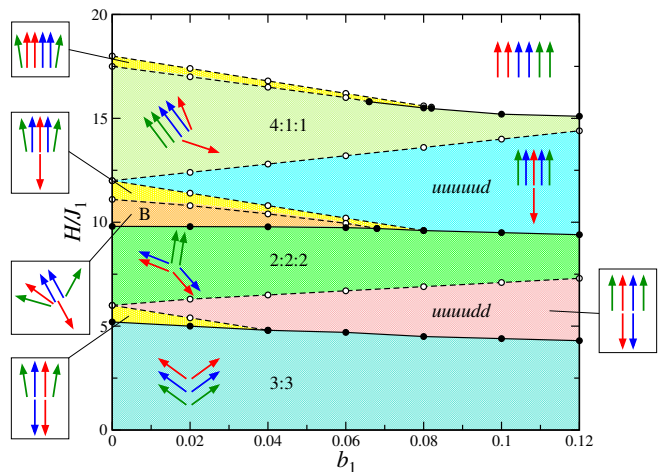


FIG. 3. Magnetic structures of a spin octahedron with a fixed ratio of biquadratic exchange constants  $b_2/b_1 = 1/2$ . Closed circles and solid lines indicate first-order transitions, open circles and dashed lines denote second-order transitions. Arrows with the same color represent spins on opposite vertices of an octahedron.

biquadratic form with  $b \propto T/J$  [47]. In addition, the magnetoelastic interaction [30] or itinerant electrons [48] may contribute to an effective biquadratic interaction in a real material.

The equilibrium spin configurations for a single octahedron are found by numerical minimization of (5) with extra biquadratic interactions (7). Results are presented in the  $H$ - $b$  phase diagram of Fig. 3. The ratio of biquadratic constants was fixed to  $1/2$  obtained above for the fully-frustrated fcc model. Generally, a negative biquadratic interaction (7) favors collinear structures among degenerate classical states. In particular, a collinear state is found in zero field, which transforms into a canted 3:3 structure for small  $H$ . A frustrated octahedron unit exhibits two additional collinear states at intermediate fields: up-up-up-up-down-down (*uuuudd*) and *uuuuud* that are stable at  $H = H_s/3$  and  $H = 2H_s/3$ , respectively. Biquadratic interactions transform the two isolated points into finite-width magnetization plateaus.

The phase diagram includes a variety of coplanar magnetic states. Their stability and occupied regions are strongly influenced by biquadratic terms. The largest number of coplanar states is present for small  $b_1$  suggesting that semiclassical, large- $S$  antiferromagnets generally have more complex phase diagrams compared to the quantum models with  $S = 1/2$  ( $b_1 = 0.083$ ) or 1 ( $b_1 = 0.041$ ). For sufficiently large  $b_1 \gtrsim 0.075$ , only three of these coplanar structures survive, 3:3, 2:2:2, and 4:1:1, all exhibiting a partial collinearity between magnetic sublattices. These states, as well as the collinear *uuuudd* and *uuuuud* structures, break the octahedron symmetry according to specific irreducible representations of the point group  $O_h$  and hence are stable with

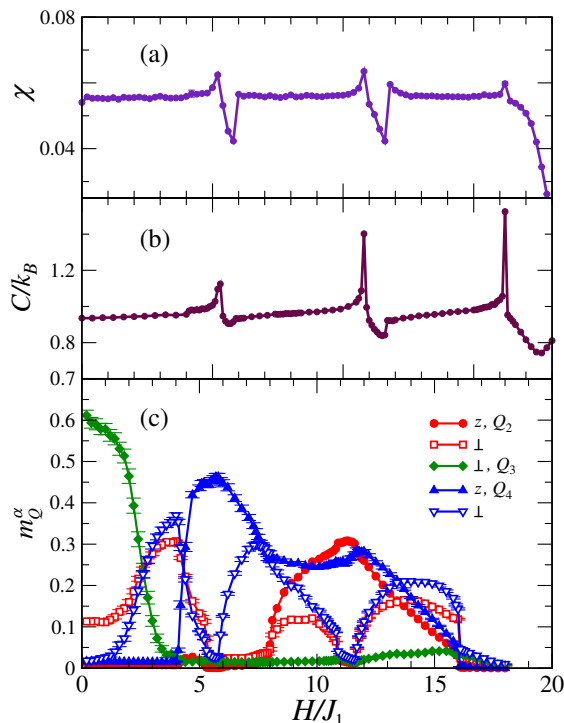


FIG. 4. Magnetic field scans from classical Monte Carlo simulations of the fully-frustrated fcc antiferromagnet ( $J_2 = J_1/2$ ) at  $T/J_1 = 0.02$ : (a) differential magnetic susceptibility  $\chi = dM/dH$ , (b) specific heat (both per spin), (c) longitudinal  $|m_Q^z|$  ( $z$ ) and transverse  $m_Q^\perp = (m_Q^x + m_Q^y)^{1/2}$  ( $\perp$ ) components of the Fourier harmonics of the antiferromagnetic order parameter, see caption of Fig. 1 and text for definitions of  $Q_n$ . The Monte Carlo results have been obtained for the  $L = 24$  cluster.

respect to additional interactions. Other values of  $b_2/b_1$  can also appear in real materials either as a result of higher-order quantum effects or due to simultaneous presence of several mechanisms for an effective biquadratic interaction. Stable spin configurations for  $b_2/b_1 = 1/4$  and 1 (relevant for the corner-shared model) are listed in End Matter together with further details on the  $H$ - $b$  diagram.

*Fully-frustrated fcc model: Monte Carlo results.* — To extend the preceding analysis based on local spin correlations, we now investigate the full effect of fluctuations in a lattice by performing the Monte Carlo (MC) simulations of the classical fully-frustrated fcc model (1). The standard Metropolis algorithm combined with the microcanonical over-relaxation steps have been used to simulate periodic clusters of linear sizes  $L = 6$ –24 with  $N = L^3$  spins. Further details on the algorithm implementation are provided in Supplemental Material [36].

Representative field scans for several physical quantities are shown in Fig. 4 for  $T/J_1 = 0.02$ . Anomalies in the differential magnetic susceptibility  $\chi = dM/dH$  and the specific heat  $C$  have been used to locate the phase

transitions. In particular, two dips in  $\chi$  at  $H_{c1} \approx 6J_1$  and  $H_{c2} \approx 12J_1$  indicate the 1/3 and 2/3 magnetization plateaus. In classical frustrated spin models,  $\chi$  typically remains finite in the plateau region instead of dropping to zero [26, 28]. Such a behavior is related to absence of a quantum gap and, hence, to a large density of gapless excitations at finite  $T$ . Presence of the collinear  $uuuudd$  and  $uuuuud$  states is clearly supported by the magnetic order parameters discussed next.

The Fourier harmonics of the antiferromagnetic order parameter

$$m_{\mathbf{q}}^\alpha = \frac{1}{N} \sum_i S_i^\alpha e^{-i\mathbf{q}\mathbf{r}_i}. \quad (8)$$

have been measured during the MC simulations. Two relevant modes are  $Q_2$  and  $Q_3$ , which correspond to zero-field states of the  $J_1$ - $J_2$  fcc antiferromagnet. Other wavevectors from the soft mode surface (4) may also contribute. In the auxiliary MC runs on small clusters ( $L = 6$ –14), we have identified another relevant harmonic corresponding to the  $G$  point with  $Q_4 = (4\pi/3, 0, 4\pi/3)$ , see Fig. 1(d). This point lies at the cross-section of the surface (4) with two mirror planes and, hence, corresponds to a high symmetry position similar to the  $L$  and  $W$  points. Due to the simultaneous importance of  $Q_3$  and  $Q_4$  modes, which possess the four- and the three-fold periodicity, we performed extensive MC simulations for two lattice sizes  $L = 12$  and 24.

Figure 4(c) shows the field dependence of antiferromagnetic modes (8), which have been summed over the star  $\{Q_n\}$  of each wavevector. In the high field region  $H/J_1 \gtrsim 3$ , the equilibrium magnetic states are composed of the harmonics that belong either to  $\{Q_2\}$  or to  $\{Q_4\}$ . At the magnetization plateaus, the transverse components of the antiferromagnetic order parameter  $m_Q^\perp = (m_Q^x + m_Q^y)^{1/2}$  vanish, whereas the longitudinal modes  $|m_Q^z|$  stay finite confirming the collinear spin configuration. The additional MC data give  $\langle |S_i^z| \rangle \approx 0.9$  at  $T/J_1 = 0.02$ , which demonstrates a fully developed longitudinal order for both magnetization plateaus [36].

The antiferromagnetic state at the 1/3 magnetization plateau consists exclusively of the  $\{Q_4\}$  harmonics. The statistical analysis of spin structures produced in the MC runs at  $H - H_{c1}$  shows that the  $uuuudd$  state has a triple- $k$  structure. In the standard representation of the fcc lattice as an  $ABC$  stack of triangular layers, the 1/3-plateau state corresponds to  $uud$  spin state in each layer, which are arranged to satisfy the 4-up/2-down constraint for every octahedron. Further details on this magnetic state as well as a real-space analysis of the  $uuuuud$  magnetic structure at the 2/3 magnetization plateau are presented in End Matter.

The  $H$ - $T$  diagram shown in Fig. 2 combines the MC results from multiple field and temperature scans. Its eight antiferromagnetic phases are labeled according to spin

configurations that are the same for all octahedral blocks in the lattice. To perform such an identification, we have used an octupole order parameter  $T^{\alpha\beta\gamma} = \langle S_i^\alpha S_i^\beta S_i^\gamma \rangle$  ( $\alpha, \beta, \gamma = x, y$ ) as well as instantaneous spin configurations, see [36]. The first-order transition lines are shown by full lines with black circles, whereas second-order transitions are indicated by dotted lines and open symbols. The dashed line inside the region of 3:3 phase corresponds to a first-order transition with a change of the ordering wavevector from  $\mathbf{Q}_2$ , at higher fields, to  $\mathbf{Q}_3$ , at lower fields. Such a transition is apparent in the field dependence of corresponding  $m_Q^{\frac{1}{3}}$  in Fig. 4(c).

The low- $T$  part of the Monte Carlo phase diagram, Fig. 2, has an apparent similarity to the  $H$ - $b$  diagram of the single-octahedron model, see Fig. 3. This is because a low- $T$  contribution from thermal fluctuations can be expressed as an effective  $T$ -dependent biquadratic coupling [47]. Nonetheless, there are a few notable differences. For example, the  $C_2$  symmetric coplanar structures present in Fig. 3 disappear completely in the MC diagram. An opposite trend affects the low-symmetry phase A, which occupies a finite region in the  $H$ - $T$  diagram, while its presence in the mean-field  $H$ - $b$  diagram is restricted to a tiny space not visible on the scale of Fig. 3, see [36].

*Discussion.* — The  $J_1$ - $J_2$  Heisenberg fcc antiferromagnet with  $J_2/J_1 = 1/2$  is an example of the fully frustrated spin model on the edge-shared octahedral lattice. The classical Monte Carlo simulations reveal its rich and complex behavior in external field with eight different antiferromagnetic phases appearing below the saturation field. A distinctive feature of the magnetic frustration in octahedron blocks is the presence of two stable magnetization plateaus at fractional values of  $m = 1/3$  and  $m = 2/3$ . For a better understanding of emergent magnetic structures, we also studied a toy model of a single spin octahedron with additional effective biquadratic exchange. The calculated phase diagram of the toy model provides an accurate guide to low temperature phases obtained in the MC study of the lattice spin model.

The fully frustrated spin octahedra can exist in the form of a corner-shared lattice in magnetic antiperovskites. In particular, the magnetization curves of  $\text{Eu}_3\text{PbO}$  and  $\text{Eu}_3\text{SnO}$  exhibit several plateau-like features [14, 15]. Further experimental work is needed to clarify their relation with magnetic frustration in the octahedral units. On the theoretical side, the  $J_1$ - $J_2$  classical spin model is highly degenerate for the corner-shared lattice of octahedra. Strong magnetic frustration for  $J_2 = J_1$  promotes the classical spin liquid states [21–23] and precludes the thermal order by disorder effect. However, similar to the previous work on the pyrochlore antiferromagnet [49], the further-neighbor exchanges can stabilize the  $q = 0$  magnetic structures making a single-octahedron physics relevant again.

Finally, the fully frustrated six-spin units that are similar but not identical to the octahedron blocks discussed

here also arise for the  $J_1$ - $J_2$ - $J_3$  antiferromagnet on a honeycomb lattice for a special relation between three exchange constants [50, 51]. Overall, our results illustrate new interesting aspects of magnetic frustration in octahedral lattices.

*Acknowledgments.* — We thank M. Gingras, H. Takagi, and A. Zelenskiy for useful discussions. The work of ASG was financially supported by the French Research Agency (ANR) within the Project Fresco, No. ANR-20-CE30-0020. MEZ acknowledges a partial support by the ANR Project Fragment, Project No. ANR-19-CE30-0040.

- 
- [1] *Magnetic systems with competing interactions (Frustrated spin systems)*, edited by H. T. Diep (World Scientific, Singapore, 1994).
  - [2] *Introduction to Frustrated Magnetism: Materials, Experiments, Theory*, edited by C. Lacroix, P. Mendels, and F. Mila (Springer-Verlag, Berlin Heidelberg, 2011).
  - [3] Y. Zhou, K. Kanoda, and T.-K. Ng, Quantum spin liquid states, *Rev. Mod. Phys.* **89**, 025003 (2017).
  - [4] L. Savary and L. Balents, Quantum spin liquids: a review, *Rep. Prog. Phys.* **80**, 016502 (2017).
  - [5] C. Broholm, R. J. Cava, S. A. Kivelson, D. G. Nocera, M. R. Norman, T. Senthil, Quantum spin liquids, *Science* **367**, 263 (2020).
  - [6] S. Deng, H. Wang, L. He, and C. Wang, Magnetic structures and correlated physical properties in antiperovskites, *Microstructures* **3**, 2023044 (2023).
  - [7] Y. Wang, H. Zhang, J. Zhu, X. Lü, S. Li, R. Zou, and Y. Zhao, Antiperovskites with Exceptional Functionalities, *Adv. Mater.* **32**, 1905007 (2020).
  - [8] H. K. Singh, Z. Zhang, I. Opahle, D. Ohmer, Y. Yao, and H. Zhang, High-Throughput Screening of Magnetic Antiperovskites, *Chem. Mater.* **30**, 6983 (2018).
  - [9] E. Krén, G. Kádár, L. Pál, J. Sólyom, P. Szabó, and T. Tarnóczy, Magnetic Structures and Exchange Interactions in the Mn-Pt System, *Phys. Rev.* **171**, 574 (1968).
  - [10] I. Tomeno, H. N. Fuke, H. Iwasaki, M. Sashiki, and Y. Tsunoda, Magnetic neutron scattering study of ordered  $\text{Mn}_3\text{Ir}$ , *J. Appl. Phys.* **86**, 3853 (1999).
  - [11] M. S. Seehra and T. M. Giebultowicz, Magnetic structures of fcc systems with nearest-neighbor and next-nearest-neighbor exchange interactions, *Phys. Rev. B* **38**, 11898 (1988).
  - [12] K. Takenaka, T. Inagaki and H. Takagi, Conversion of magnetic structure by slight dopants in geometrically frustrated antiperovskite, *Appl. Phys. Lett.* **95**, 132508 (2009).
  - [13] E. Matsuoka, A. Oshima, H. Sugawara, T. Sakurai, and H. Ohta, Possible Frustration Effects on a New Antiferromagnetic Compound  $\text{Ce}_6\text{Pd}_{13}\text{Zn}_4$  with the Octahedral Ce Sublattice, *J. Phys. Soc. Jpn.* **87**, 013705 (2018).
  - [14] M. M. Hirschmann, A. S. Gibbs, F. Orlandi, D. Khalayavin, P. Manuel, V. Abdolazimi, A. Yaresko, J. Nuss, H. Takagi, A. P. Schnyder, and A. W. Rost, Creating and controlling Dirac fermions, Weyl fermions, and nodal lines in the magnetic antiperovskite  $\text{Eu}_3\text{PbO}$ , *Phys. Rev. Mater.* **6**, 114202 (2022).
  - [15] M. Li, D. Han, Z. Wang, B. Li, T. Yang, Zh. Zhang, F.

- Gao, H. Wang, X. Zhao, D. Li, and Z. Zhang, Magnetic and transport properties in antiferromagnetic antiperovskite  $\text{Eu}_3\text{SnO}$ , *Phys. Rev. Mater.* **7**, 074203 (2023).
- [16] D. G. Franco, R. Avalos, D. Hafner, K. A. Modic, Yu. Prots, O. Stockert, A. Hoser, P. J. W. Moll, M. Brando, A. A. Aligia, and C. Geibel, Frustrated magnetism in octahedra-based  $\text{Ce}_6\text{Ni}_6\text{P}_{17}$ , *Phys. Rev. B* **109**, 054405 (2024).
- [17] D. Tahara, Y. Motome, and M. Imada, Antiferromagnetic Ising Model on Inverse Perovskite Lattice, *J. Phys. Soc. Jpn.* **76**, 013708 (2007).
- [18] V. Hemmati, M. L. Plumer, J. P. Whitehead, and B. W. Southern, Monte Carlo simulations of magnetic ordering in the fcc kagome lattice, *Phys. Rev. B* **86**, 104419 (2012).
- [19] S. R. Sklan, and C. L. Henley, Nonplanar ground states of frustrated antiferromagnets on an octahedral lattice, *Phys. Rev. B* **88**, 024407 (2013).
- [20] M. D. LeBlanc, M. L. Plumer, J. P. Whitehead, and B. W. Southern, Monte Carlo simulations of the fcc kagome lattice: Competition between triangular frustration and cubic anisotropy, *Phys. Rev. B* **88**, 094406 (2013).
- [21] O. Benton and R. Moessner, Topological Route to New and Unusual Coulomb Spin Liquids, *Phys. Rev. Lett.* **127**, 107202 (2021).
- [22] A. Szabo, F. Orlandi, and P. Manuel, Fragmented Spin Ice and Multi-k Ordering in Rare-Earth Antiperovskites, *Phys. Rev. Lett.* **129**, 247201 (2022).
- [23] J. A. M. Paddison and M. J. Cliffe, Discovering classical spin liquids by topological search of high symmetry nets, *ACS Cent. Sci.* **10**, 1821 (2024).
- [24] M. E. Zhitomirsky, A. Honecker, and O. A. Petrenko, Field Induced Ordering in Highly Frustrated Antiferromagnets, *Phys. Rev. Lett.* **85**, 3269 (2000).
- [25] D. H. Lee, J. D. Joannopoulos, J. W. Negele, and D. P. Landau, Discrete-Symmetry Breaking and Novel Critical Phenomena in an Antiferromagnetic Planar ( $XY$ ) Model in Two Dimensions, *Phys. Rev. Lett.* **52**, 433 (1984).
- [26] H. Kawamura and S. Miyashita, Phase Transition of the Heisenberg Antiferromagnet on the Triangular Lattice in a Magnetic Field, *J. Phys. Soc. Jpn.* **54**, 4530 (1985).
- [27] A. V. Chubukov and D. I. Golosov, Quantum theory of an antiferromagnet on a triangular lattice in a magnetic field, *J. Phys.: Condens. Matter* **3**, 69 (1991).
- [28] M. E. Zhitomirsky, Field-Induced Transitions in a Kagomé Antiferromagnet, *Phys. Rev. Lett.* **88**, 057204 (2002).
- [29] J. Schulenburg, A. Honecker, J. Schnack, J. Richter, and H.-J. Schmidt, Macroscopic Magnetization Jumps due to Independent Magnons in Frustrated Quantum Spin Lattices, *Phys. Rev. Lett.* **88**, 167207 (2002).
- [30] K. Penc, N. Shannon, and H. Shiba, Half-Magnetization Plateau Stabilized by Structural Distortion in the Antiferromagnetic Heisenberg Model on a Pyrochlore Lattice, *Phys. Rev. Lett.* **93**, 197203 (2004).
- [31] M. E. Zhitomirsky and H. Tsunetsugu, Lattice gas description of pyrochlore and checkerboard antiferromagnets, *Phys. Rev. B* **75**, 224416 (2007).
- [32] S. Nishimoto, N. Shibata, and C. Hotta, Controlling frustrated liquids and solids with an applied field in a kagome Heisenberg antiferromagnet, *Nat. Commun.* **4**, 2287 (2013).
- [33] S. Capponi, O. Derzhko, A. Honecker, A. M. Läuchli, and J. Richter, Numerical study of magnetization plateaus in the spin-1/2 kagome Heisenberg antiferromagnet, *Phys. Rev. B* **88**, 144416 (2013).
- [34] T. Picot, M. Ziegler, R. Orus, and D. Poilblanc, Spin- $S$  kagome quantum antiferromagnets in a field with tensor networks, *Phys. Rev. B* **93**, 060407(R) (2016).
- [35] E. F. Bertaut, D. Fruchart, J. P. Bouchaud, and R. Fruchart, Diffraction neutronique de  $\text{Mn}_3\text{GaN}$ , *Solid State Commun.* **6**, 251 (1968).
- [36] See Supplemental Material for details on the classical ground state degeneracy, the phase diagram of the single octahedron model, the Monte Carlo results on the fully frustrated fcc model.
- [37] R. Moessner and J. T. Chalker, Low-temperature properties of classical geometrically frustrated antiferromagnets, *Phys. Rev. B* **58**, 12049 (1998).
- [38] A. B. Harris, C. Kallin, and A. J. Berlinsky, Possible Néel orderings of the Kagome antiferromagnet, *Phys. Rev. B* **45**, 2899 (1992).
- [39] M. E. Lines, Green Functions in the Theory of Antiferromagnetism, *Phys. Rev.* **135**, A1336 (1964).
- [40] M. T. Heinilä and A. S. Oja, Long-range order produced by the interaction between spin waves in classical fcc Heisenberg models, *Phys. Rev. B* **48**, 16514 (1993).
- [41] P. Balla, Y. Iqbal, and K. Penc, Degenerate manifolds, helimagnets, and multi- $Q$  chiral phases in the classical Heisenberg antiferromagnet on the face-centered-cubic lattice, *Phys. Rev. Research* **2**, 043278 (2020).
- [42] J. Villain, R. Bidaux, J.-P. Carton, and R. Conte, Order as an effect of disorder, *J. de Physique* **41**, 1263 (1980).
- [43] E. F. Shender, Antiferromagnetic garnets with fluctuationally interacting lattices, *Zh. Éksp. Teor. Fiz.* **83**, 326 (1982) [*Sov. Phys. JETP* **56**, 178 (1982)].
- [44] C. L. Henley, Ordering due to disorder in a frustrated vector antiferromagnet, *Phys. Rev. Lett.* **62**, 2056 (1989).
- [45] M. T. Heinilä and A. S. Oja, Selection of the ground states in the type-I fcc antiferromagnets in an external magnetic field, *Phys. Rev. B* **48**, 7227 (1993).
- [46] M. E. Zhitomirsky, Real-space perturbation theory for frustrated magnets: application to magnetization plateaus, *J. Phys.: Conf. Series* **592**, 012110 (2015).
- [47] B. Canals and M. E. Zhitomirsky, An  $XY$  checkerboard antiferromagnet in an external field, *J. Phys.: Condens. Matter* **16**, S759 (2004).
- [48] A. L. Wysocki, K. D. Belashchenko, L. Ke, M. van Schilfgaarde, and V. P. Antropov, Biquadratic magnetic interaction in parent ferropnictides, *J. Phys.: Conf. Series* **449**, 012024 (2013).
- [49] N. Shannon, K. Penc, and Y. Motome, Nematic, vector-multipole, and plateau-liquid states in the classical  $O(3)$  pyrochlore antiferromagnet with biquadratic interactions in applied magnetic field, *Phys. Rev. B* **81**, 184409 (2010).
- [50] J. Rehn, A. Sen, K. Damle, and R. Moessner, Classical Spin Liquid on the Maximally Frustrated Honeycomb Lattice, *Phys. Rev. Lett.* **117**, 167201 (2016).
- [51] F. A. G. Albarracin and H. D. Rosales, Multiple pseudo-plateau states and antiferromagnetic pair selection in the  $XY$  model in the highly frustrated honeycomb lattice, *J. Phys.: Condens. Matter* **33**, 185801 (2021).

## End Matter

*Appendix: Single octahedron states.* — To verify the stability and ubiquity of the coplanar magnetic structures found previously for  $b_2/b_1 = 1/2$ , we have performed additional numerical minimization of the single octahedron energy for other values of two biquadratic constants. Figure 5 shows the magnetization curves  $M(H)$ , the differential susceptibility  $dM/dH$  (upper panel) and field-induced states phases (lower panel) for  $b_1 = 0.02$  and  $b_2/b_1 = 1/4, 1/2$ , and 1. The magnetization curves are very similar exhibiting two magnetization plateaus of similar width. The case  $b_2 = b_1$  has an additional symmetry and its sequence of field-induced states is discussed separately. Overall, there is a remarkable similarity between field-induced magnetic states for all  $b_2 < b_1$ . Six states, 4:1:1,  $uuuuud$ , 2:1:1:1, 2:2:2,  $uuudd$ , and 3:3 (from top to bottom), are common for both  $b_2/b_1 = 1/4$  and  $1/2$ . The remaining differences can be understood from the following analytical analysis.

For the Heisenberg model, spin and lattice rotations are uncoupled and the full symmetry group of the system is  $G = O_h \times U(1)$ . The fully polarized  $uuuuuu$  state at high fields remains invariant under all symmetry operations of  $G$ . The transition field  $H_s$  into a canted antiferromagnetic state can be determined analytically by expanding the energy in transverse spin components and diagonalizing the corresponding quadratic form:

$$H_s = 6J_1(3 - 8b_1 - 4b_2). \quad (\text{A1})$$

This second-order transition corresponds to the three-dimensional  $T_{1u}$  representation of  $O_h$ . The symmetry of the antiferromagnetic state below  $H_s$  is determined by nonlinear quartic terms in the energy expansion. One can show analytically that an effective ‘cubic’ anisotropy in the Landau functional for the  $T_{1u}$  mode changes sign at  $b_2 = 0.4b_1$ . Consequently, for  $b_2 < 0.4b_1$  the lowest energy state has equal amplitudes for the three  $T_{1u}$  eigenstates and corresponds to the 3:3 canted structure. For  $b_2 > 0.4b_1$ , only one component of the  $T_{1u}$  triplet condenses, producing the 4:1:1’ state, see Fig. 5.

A similar analysis can be performed separately for each of the magnetization plateaus. The  $uuuuud$  state of the 2/3 plateau preserves  $G' = C_{4v} \times U(1)$  symmetry. The upper and lower plateau boundaries are given, respectively, by

$$\begin{aligned} H_{c_2}^{(2/3)} &= 12J_1(1 + \sqrt{17b_1^2 + 8b_1b_2 - b_1}), \\ H_{c_1}^{(2/3)} &= 12J_1(1 - 4b_1 - 2b_2). \end{aligned} \quad (\text{A2})$$

The instability at the upper edge of the plateau is determined by a single mode that transforms as  $A_1$  irrep of  $C_{4v}$ . At the lower edge, a two-component mode of the  $E$  irrep condenses. Again, we find the mixed two-component  $E$  state 2:2:1:1’ for  $b_2 < 4b_1/9$ , whereas

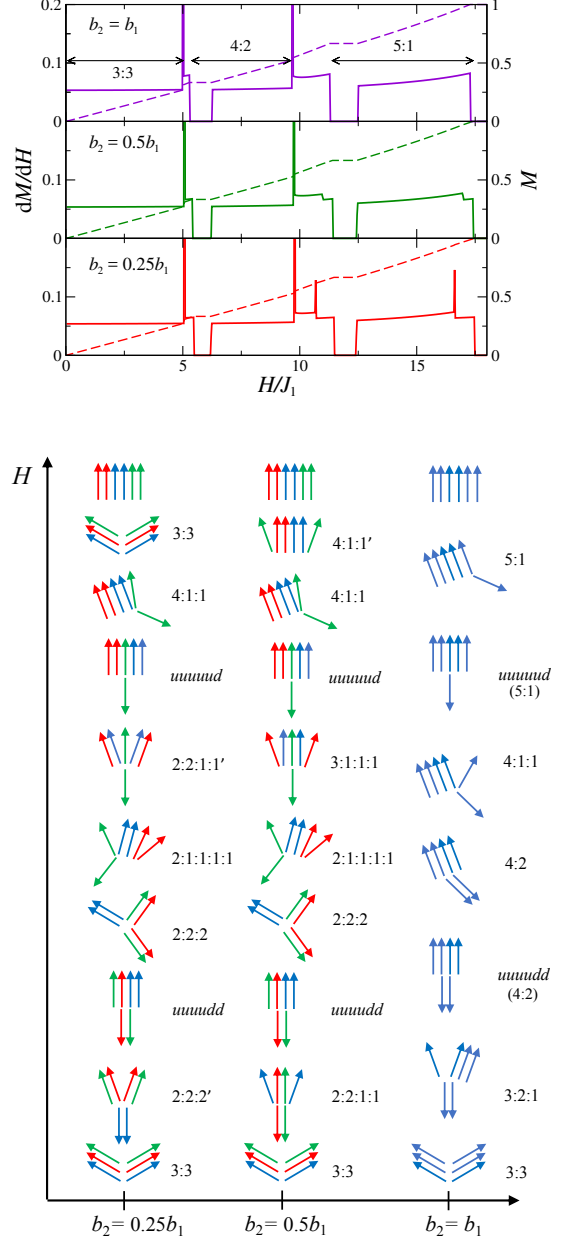


FIG. 5. Upper panel: the magnetization curves  $M(H)$  (dashed lines) and the differential susceptibility  $dM/dH$  (solid lines) versus field for  $b_1 = 0.02$  and varying  $b_2/b_1$ . Lower panel: Graphical representation of stable spin configurations in various fields. Same color vectors for  $b_2/b_1 < 1$  indicate spins on the opposite vertices of an octahedron.

the single-component  $E$  state 3:1:1:1 is energetically stable for  $b_2 > 4b_1/9$ . Similarly, for the 1/3 magnetization plateau we find

$$\begin{aligned} H_{c_2}^{(1/3)} &= 6J_1[1 + 4\sqrt{b_1(3b_1 + b_2)} - 4b_1], \\ H_{c_1}^{(1/3)} &= 6J_1(1 - 8b_1 - 4b_2). \end{aligned} \quad (\text{A3})$$

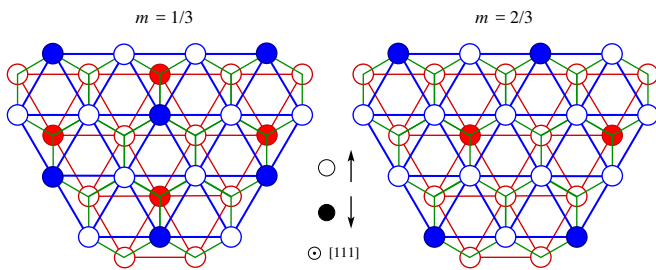


FIG. 6. The high symmetry magnetic structures for the 1/3 (left panel) and the 2/3 (right panel) magnetization plateaus. The fcc lattice is represented as an  $ABC$  stack of triangular layers of magnetic ions. Two such adjacent layers are shown by blue (upper layer) and red (lower layer) balls. Octahedron spin blocks are formed between the layers and are indicated by green hexagons.

Note that the  $C_2$  symmetric coplanar structures found below the collinear states in the energetic analysis disappear completely in the MC simulations at finite temperatures. Accordingly, Fig. 2 shows direct first-order transitions into the less symmetric structures.

The symmetry of a single spin octahedron is enhanced for equal biquadratic constants  $b_2 = b_1$ . There is no longer a distinction between edge and diagonal bonds of an octahedron. Accordingly, the block Hamiltonian is symmetric with respect to all permutations of six spins, which form the group  $S_6$ . Stable magnetic structures obtained in this case are shown in Fig. 5. A partial collinearity in these canted spin structures becomes even more apparent. In fact, magnetic states found for  $b_2 = b_1$  belong to different irreducible representations of  $S_6$  that are described by the Young diagrams. This is emphasized by the chosen notations for the coplanar spin configurations, which list the number of boxes in each row of the corresponding Young diagram. Interestingly, the high-field 4:1:1 state present for  $b_2 < b_1$  is obtained by an appropriate spin distortion from the 5:1 state found for  $b_2 = b_1$ . Such a relation explains why the low-symmetry 4:1:1 state has a wide range of stability for different  $b_2/b_1$  as well as for a varying  $b_1$ , see Fig. 3.

*Appendix: Magnetization plateau structures.* — Here we provide further details on the spin configurations obtained in the Monte Carlo simulations for two magnetization plateaus of the fully-frustrated fcc model. It is convenient to represent an fcc lattice by the  $ABC$  stacking of triangular planes of magnetic atoms along the [111] crystal axis. Figure 6 shows two such adjacent triangular layers. The octahedral blocks in the three-dimensional fcc

lattice correspond to two overlapping triangles in the adjacent layers of Fig. 6 with the interlayer exchange bonds forming hexagons. The up and down spins in the magnetic structures are shown by the open and filled circles.

For the lower, 1/3 magnetization plateau, every layer has the  $\sqrt{3} \times \sqrt{3}$  superstructure of down spins similar to the triangular-lattice antiferromagnet. Thus, every layer has the  $C_3$  rotation symmetry around the [111] axis. The classical constraint for the 1/3 magnetization plateau requires presence of two down spins (filled circles) for each octahedron. This is achieved by selecting a down spin in the top  $A$  layer and placing another down spin on the triangular plaquette of the adjacent  $B$  layer that surrounds the filled circle (down spin), see the left panel of Fig. 6. Once one of the three vertices is chosen as a filled circle, the remaining spin configuration in this layer becomes also fixed. A similar three-fold choice must be again made for the third  $C$  layer and so on. As a result a proper  $uuudd$  magnetic structure can be constructed in at least  $3^{L_p}$  different ways, where  $L_p$  is the number of triangular planes in the fcc lattice. The most symmetric state is obtained once down spins in the adjacent layers form parallel columns (rows) when viewed along the [111] direction. This symmetric state exhibits the period-3 structure along the [111] axis such that every  $A$ ,  $B$ , or  $C$  layer has the same configuration of up and down spins. Overall, the  $C_3$  rotation symmetry is broken and the magnetic state is described by a superposition of three Fourier harmonics from the star  $\{Q_4\}$  such that one amplitude is twice larger than two others.

For the upper magnetization plateau, the density of down spins in every triangular layer must be twice smaller compared to the 1/3 plateau. This is achieved by placing up-down spin on every third chain in a triangular layer, while two intermediate spin chains remain fully polarized (uncolored), see the right panel of Fig. 6. By performing such a coloring we select one of two possible up-down structures. This yields the  $2^{L_c}$  configuration degeneracy,  $L_c$  being the number of parallel chains in one layer. Once a choice of down spins is made in the entire  $A$  layer, the classical constraint selects uniquely the down spins in the adjacent  $B$  layer and so on. The most symmetric pattern has a six-fold periodicity in the direction orthogonal to the up-down chain. The same six-fold periodicity arises in the [111] direction perpendicular to triangular planes. Because of its mixed six- and two-fold periodicity, such a magnetic structure has non-zero Fourier harmonics from the stars of both  $\{Q_2\}$  and  $\{Q_4\}$ . Specifically, the  $uuuud$  spin structure of the 2/3 magnetization plateau is composed of one  $Q_2$  mode and three  $Q_4$  modes.